

In-situ selective surface engineering of graphene micro-supercapacitor chips

Yiming Chen^{1,§}, Minghao Guo^{1,§}, Lin Xu^{1,2} (✉), Yuyang Cai¹, Xiacong Tian^{1,3}, Xiaobin Liao¹, Zhaoyang Wang¹, Jiashen Meng¹, Xufeng Hong¹, and Liqiang Mai^{1,2} (✉)

¹ State Key Laboratory of Advanced Technology for Materials Synthesis and Processing, Wuhan University of Technology, Wuhan 430070, China

² Foshan Xianhu Laboratory of the Advanced Energy Science and Technology Guangdong Laboratory, Xianhu Hydrogen Valley, Foshan 528200, China

³ Faculty of Materials Science & Chemistry, China University of Geosciences, Wuhan 430074, China

[§] Yiming Chen and Minghao Guo contributed equally to this work.

© Tsinghua University Press and Springer-Verlag GmbH Germany, part of Springer Nature 2021

Received: 11 April 2021 / Revised: 7 June 2021 / Accepted: 16 June 2021

ABSTRACT

Surface modification of graphene oxide (GO) is a powerful strategy to develop its energy density for electrochemical energy storage. However, pre-modified GO always exhibits unsatisfactory hydrophilia and its ink-relevant utilization is extremely limited. Although GO ink is widely utilized in fabricating micro energy storage devices via extrusion-based 3D-printing, simultaneously obtaining satisfactory hydrophilia and high energy density still remains a challenge. In this work, an *in-situ* surface engineering strategy was employed to enhance the performance of GO micro-supercapacitor chips. Three dimensionally printed GO micro-supercapacitor chips were treated with pyrrole monomer to achieve selective and spontaneous anchoring of polypyrrole on the microelectrodes without affecting interspaces between the finger electrodes. The interface-reinforced graphene scaffolds were edge-welded and exhibited a considerably improved specific capacitance, from 13.6 to 128.4 mF·cm⁻². These results are expected to provide a new method for improving the performance of micro-supercapacitors derived from GO inks and further strengthen the practicability of 3D printing techniques in fabricating energy storage devices.

KEYWORDS

3D-printing, *in-situ* modification, selective surface engineering, edge-welded graphene, micro-supercapacitors

1 Introduction

In recent years, because of the tremendous demand for miniaturized, flexible and highly integrated electronic products, there is an urgent need to develop sustainable and environmentally friendly micro energy storage devices (MESDs), including micro-batteries and micro-supercapacitors (MSCs) [1–8]. As an emerging effective additive manufacturing approach to fabricate three-dimensional (3D) architectures, the extrusion-based 3D printing technique has become increasingly prominent [9–13]. The 3D-printed MESDs are constructed by multilayer filaments where the devices can be configured into desired 3D structure and areal mass loading can be effectively improved by piling up the filaments [14–16]. Customized 3D structure ensures controllable regulation of electrochemical processes (ion diffusion and reaction kinetic) and performance (areal energy density, rate performance, potentials of electro-catalysis, etc.) [17–19]. This additive manufacturing achieves fast and precise fabrication with minimal waste of primary materials [20–22]. Additionally, flexible material utilization (GO [15, 16, 23–40], MXene [41–45], cellulose [46], et al.) allows numerous choices for electrochemical energy storage and conversion systems [17, 47–49].

As a prominent type of printable inks, GO suspension is widely utilized in 3D-printing to fabricate MSCs [50]. The

prepared GO ink exhibits proper rheological property, then the fabricated MSCs generally have high power density and superior cycling stability. Li et al. fabricated all-reduced graphene oxide (rGO)-MSCs employing pure graphene oxide (GO) ink via 3D printing. They obtained controllable electrochemical performance by configuring the porous structures and macroscopic constructions of the microelectrodes [27]. However, the fabricated MSCs suffer from limited intrinsic capacitance of the graphene flakes and exhibit restricted performance (Fig. 1(a)). According to previous reports, one of the most effective strategies to improve the electrochemical performance of graphene-based electrodes is surface modification, as it is powerful to incorporate high-mass-loaded active materials with large surface area, which may contribute a lot to capacitive energy storage [18, 51–54]. However, the modified GO flakes always exhibit unsatisfactory hydrophilia and their ink-related utilization is extremely limited (Fig. 1(b)). Hence, simultaneously obtaining high energy density and excellent printing-feasibility remains a challenge.

To address above issues, an on-chip *in-situ* selective surface engineering strategy is proposed in this study to achieve self-induced modification of GO-based micro-patterns. This strategy combines the printing-feasibility of GO ink and performance optimization of surface engineering. These characteristics can

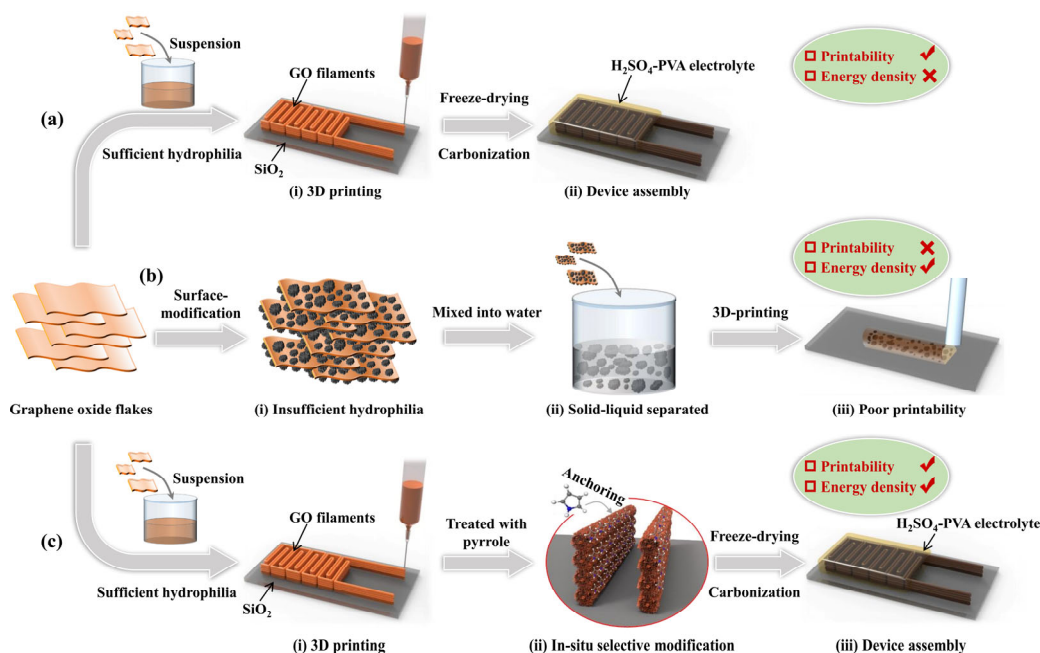


Figure 1 Schematic illustration of the fabricating process for 3D printed microelectrodes. (a) Printing with GO ink: (i) Fabrication of GO micro-patterns via extrusion-based 3D printing. (ii) Freeze-drying and pyrolysis of the obtained micro-patterns to prepare MSC-rGO. (b) Printing with pre-modified GO ink: (i) Modified GO flakes with insufficient hydrophilia exhibit (ii) solid-liquid separated state after mixing into water. (iii) The obtained ink exhibits poor printability. (c) Printing with GO ink followed by post-modification: (i) Fabrication of GO micro-patterns via extrusion-based 3D printing. (ii) Immersion of GO micro-patterns into liquid pyrrole to achieve in-situ modification. (iii) Freeze-drying and pyrolysis of the obtained micro-patterns to prepare MSC-NC/rGO.

be used to develop a unique morphology resulting from this in-situ engineering and obtain considerable capacitance via the incorporation of N source. In this work, the self-induced reaction of GO and pyrrole was utilized in fabricating MSCs, and additional substances such as ferric chloride (FeCl_3) or ammonium persulfate were not required (Fig. 1(c)). This strategy avoids affecting interspaces between the finger electrodes and incorporation of impurities [55–58]. The interface-reinforced samples presented edge-welded-graphene-based structure and exhibited enhanced performance. The MSC with 6 layers treated for 1 week delivered a total nitrogen doping level of 5.74% and exhibited a specific areal capacitance of $128.4 \text{ mF}\cdot\text{cm}^{-2}$, around 9 times that of the untreated chips. Since GO is widely employed in MESDs, this *in-situ* selective interface engineering strategy opens a new avenue for optimizing the performance of GO-based MESDs.

2 Experimental

2.1 Preparation of inks

GO was synthesized by the modified Hummer's method. To prepare condensed GO suspension, 375 mg GO particles were dissolved into 5 mL distilled (DI) water under continuous stirring for 3 h, ultrasonication for 30 min and repeated for 3 times. Stable ink with suitable rheological property can be prepared. To prepare contrast sample, GO flakes treated by pyrrole for 6 h were mixed into water with the same condition, denoted as GO-pyrrole ink.

2.2 3D printing of GO micro-patterns

An extrusion-based 3D printing system (BIO-X (CELLINK)) was utilized for the printing process. The GO ink was housed in a 3 mL syringe attached by a stainless micronozzle (inner diameter: $150 \mu\text{m}$). To create 3D interdigital microelectrodes, fine filaments were extruded directly from a nozzle while the piston is being propelled by motor. With a typical printing speed

of $3 \text{ mm}\cdot\text{s}^{-1}$, the filaments were then deposited layer-by-layer on the glass substrate ($18 \text{ mm} \times 18 \text{ mm}$) following a preprogrammed printing routine.

2.3 Surface engineering of the microelectrode chips

The printed micro-patterns were soaked in liquid pyrrole (99.7%, Aladdin) at room temperature for 6, 24 h, 4 days, 1 week and 2 weeks to realize the self-induced reaction. Afterwards, the chips were washed by ethanol and water, respectively for 3 times to remove the unpolymerized pyrrole monomer. Then they were frozen in the refrigerator ($-40 \text{ }^\circ\text{C}$) and freeze-dried for 24 h to obtain 3D architectures. To obtain the nitrogen-doped carbon (NC)/rGO electrodes, the samples were carbonized under $800 \text{ }^\circ\text{C}$ in N_2 atmosphere for 2 h (heating rate: $2 \text{ }^\circ\text{C}\cdot\text{min}^{-1}$).

2.4 Materials characterization

SEM images were observed using a JEOL-7100F field-emission SEM at an acceleration voltage of 20 kV. The transmission electron microscopy (TEM) image was collected using a Titan G2 60-300 Probe Cs Corrector HRSTEM. Fourier transform infrared (FT-IR) were measured using a Nicolet 6700 IR spectrometer (Thermo Fisher Scientific Co., USA). After the treated samples were pressed into relatively thin films. X-ray diffraction (XRD) patterns were recorded via a D8 discover X-ray diffractometer with $\text{Cu K}\alpha$ radiation. Raman spectrum was measured using a LabRAM HR Evolution & Smart SPM. XPS spectra were recorded using a VG Multilab 2000. Nitrogen content was tested using an Elemental Analyzer (Model: Vario EL cube). All of the electrochemical tests were conducted using an Autolab PGSTAT302N or CHI760D electrochemical workstation.

2.5 Electrochemical measurements

All of the electrochemical measurements were conducted using a two electrodes system utilizing H_2SO_4 -PVA electrolyte.

Both the cyclic voltammetry (CV) tests and GCD tests were delivered at the potential window from 0 to 1 V. Electrochemical impedance spectroscopy (EIS) tests were achieved at the frequency from 0.01 to 5×10^5 Hz. The specific areal capacitance was calculated from GCD curves, according to the following equation [59]:

$$C_{\text{areal}} = \frac{I\Delta t}{A\Delta V} \quad (1)$$

In which I (A) is the total current, Δt (s) refers to the discharge time, A (cm^2) represents the foot print area of the interdigital patterns, ΔV (V) is the potential window of discharge. To calculate energy density and power density, the following equations were used:

$$E_{\text{areal}} = \frac{C_{\text{areal}}\Delta V^2}{7200} \quad (2)$$

$$P_{\text{areal}} = \frac{E_{\text{areal}}}{\Delta t} \times 3,600 \quad (3)$$

In which C_{areal} is the specific areal capacitance, ΔV is the potential window of discharge and Δt is the discharge time.

3 Results and discussion

The fabricating process of MSCs used in this study is shown in Fig. 1(c). Owing to the abundant oxygen-related functional groups, GO showed superior hydrophilia, which enabled the preparation of concentrated GO suspension inks to facilitate the layer-by-layer accumulation in the 3D printing technique. To evaluate the printability, rheological tests of GO ink were conducted (shown in Figs. S1(a) and S1(b) in the Electronic Supplementary Material (ESM)). Subsequently, the GO ink was

directly printed on the glass substrate layer by layer following the programmed route, the obtained micro-patterns are shown in Figs. S1(c) and S1(d) in the ESM. As GO is in an oxidation state, it can polymerize pyrrole monomer into PPy. On account of this, the microelectrode chips were immersed into liquid pyrrole to realize the self-induced reaction. After PPy was anchored on the surface of graphene (GO was also partly reduced, denoted as p-rGO), freeze-drying was used to prevent the collapse and construct 3D p-rGO@PPy architectures. The obtained samples were washed using ethanol and water for 3 times to remove the un-polymerized pyrrole monomer. Then, they were carbonized at 800 °C (N_2) after freeze-drying to obtain MSC-NC/rGO. The dimensions of fabricated samples with 6 layers are shown in Fig. S2 in the ESM. Figures S2(a) and S2(b) in the ESM present the sizes of finger electrodes and utilized area. Cross sectional scanning electron microscopy (SEM) image is shown in Fig. S2(c) in the ESM, all 6 layers exhibit a height of 946 μm (Fig. S2(d) in the ESM). Subsequently, the MCSs were treated using O_2 plasma to further improve the hydrophilia and facilitate the permeation of electrolyte. With H_2SO_4 -PVA electrolyte coating, the MSCs were finally fabricated. To investigate the printability of pre-modified GO-pyrrole ink, contrast experiment referred to Fig. 1(b) was conducted and comparable results with GO ink are shown in Fig. S3 in the ESM. The GO-pyrrole ink exhibited solid-liquid-separated state due to the fading of hydrophilia (Fig. S4 in the ESM) and delivered poor printability, which further manifested the advantage of in-situ selective surface engineering.

Figure 2(a) shows the adsorption of pyrrole on the GO filaments. When GO micro-patterns were immersed, pyrrole was adsorbed on the surface of GO sheets owing to the π - π interaction [60]. The self-polymerization of the pyrrole monomer

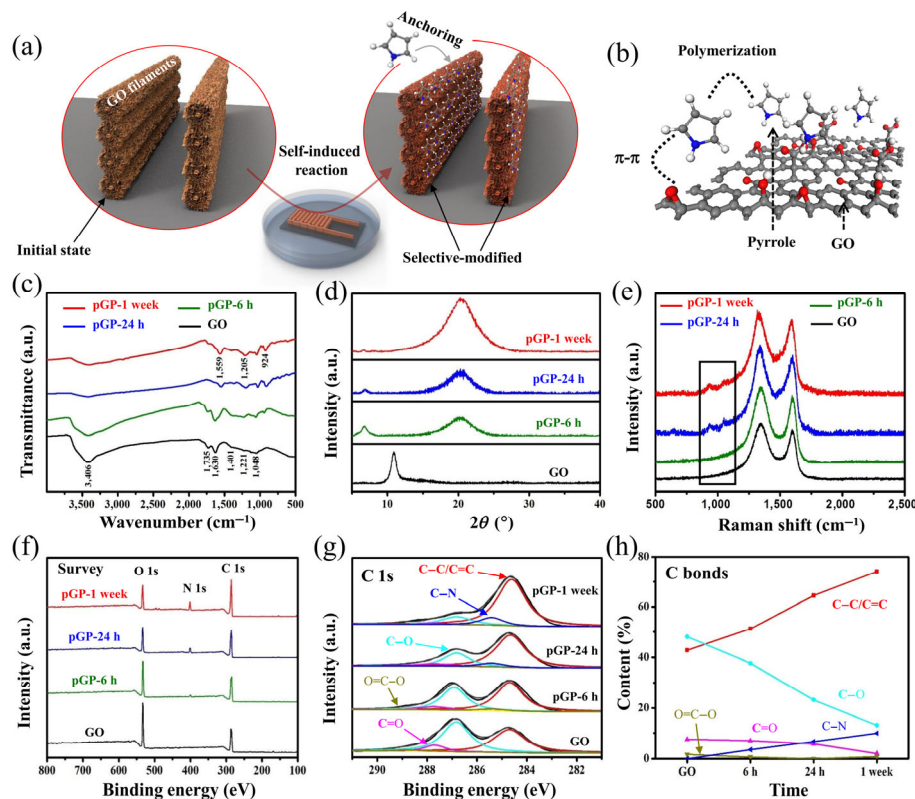


Figure 2 Schematic illustration for (a) the process of immersing micro-patterns into liquid pyrrole. (b) The interaction between GO and pyrrole monomer. (c) FT-IR spectra, (d) XRD patterns, (e) Raman spectra and (f) XPS spectra of the pristine GO, pGP-6 h, pGP-24 h and pGP-1 week. (g) High-resolution C 1s peaks of the pristine GO, pGP-6 h, pGP-24 h and pGP-1 week, including C-C/C=C (284.7 eV), C-O-C/OH (286.8 eV), C=O (287.7 eV), HO-C=O (288.9 eV) and C-N (285.4 eV). (h) The relative contents of C-C/C=C, C-O-C/OH, C=O, HO-C=O and C-N bonds in C related bonds of different samples.

was driven by the oxygen functional groups on GO, and GO was also partially reduced (p-rGO). After this self-oxidation-reduction (SOR) reaction, PPy was selectively and accurately anchored on the graphene sheets (Fig. 2(b)). Whereas, no PPy generated on the glass substrate and the remained pyrrole was removed by ethanol, which avoided the short circuit after carbonization. To clearly investigate the mechanism of the SOR reaction, the generation of PPy and the partial reduction of GO, GO micro-patterns were immersed into liquid pyrrole for different times (6, 24 h and 1 week). The obtained samples were denoted as pGP-6 h, pGP-24 h and pGP-1 week, respectively. FT-IR, XRD, Raman tests and X-ray photoelectron spectroscopy (XPS) were conducted to detect the evolution of the functional groups.

The FT-IR spectra of these four samples are shown in Fig. 2(c). Two strong bands located at ca. 1,630 and 3,406 cm^{-1} can be observed in the spectrum of GO, representing C=C and O-H stretching vibrations, respectively. The peaks at ca. 1,735, 1,048 and 1,401 cm^{-1} reflect the strong C=O stretching vibration in carbonyl moieties/carboxylic acid, C-O stretching vibration in epoxy group and C-O stretching vibration in carboxylic acid, respectively. The peak at ca. 1,221 cm^{-1} refers to C-OH stretching vibration [61]. As the immersion time increased, the intensities of the peaks associated with the O-H stretching vibration (ca. 3,406 cm^{-1}), C=O stretching vibration in carbonyl moieties and carboxylic acid (ca. 1,735 cm^{-1}), C=C stretching vibration (ca. 1,630 cm^{-1}) and carboxy C-O stretching vibration (ca. 1,401 cm^{-1}) gradually approached zero. This suggests the extensive removal of C-OH and carboxy C-OH groups as well as the partial reduction of GO. In the meantime, several new peaks at ca. 924, 1,205 and 1,559 cm^{-1} appeared, which respectively represented the out-of-plane deformation vibration of C-H band, N-H stretching vibration and antisymmetric pyrrole-ring stretching vibration. This further indicated the polymerization of pyrrole monomer by interacting with hydroxyl and carboxyl groups [62–64].

Figure 2(d) shows the XRD patterns of pGP-6 h, pGP-24 h and pGP-1 week in comparison with the pristine GO micro-patterns. In the spectrum of the pristine GO, a typical broad peak at $2\theta = 10.89^\circ$ (d -spacing = 8.14 Å) can be observed [65]. After immersed in liquid pyrrole, the diffraction angle slightly decreases, indicating the increased d -spacing. This is possibly caused by the insertion of PPy chain into the interlayer of some GO sheet. In the same way, the weakening and disappearance of the (002) peak occurred during the longer reaction time, indicating the partially amorphization of the graphene sheets. A broad band appeared at around 20° and became stronger with longer treating time, this might be because some GO was also partially reduced by pyrrole and obtained decreased d -spacing [61].

Raman spectra (Fig. 2(e)) of the pristine GO, pGP-6 h, pGP-24 h and pGP-1 week were also obtained. It's obvious that the pristine GO exhibits typical D band (ca. 1,342 cm^{-1}) and G band (ca. 1,596 cm^{-1}), representing defects/disordered carbon and ordered sp^2 -bonded carbon, respectively [66]. To obviously observe the small peaks located at 800–1,200 cm^{-1} , fitting curves were drawn (shown in Fig. S5 in the ESM). Peaks at 930, 980 and 1,050 cm^{-1} can be identified, the peaks at 930 and 980 cm^{-1} are respectively associated with the bipolaron and polaron structure of PPy [67]. The intensity of these peaks gradually increased over the treatment time, which demonstrates the improved polymerized extent of PPy.

The XPS survey spectra of pristine GO, pGP-6 h, pGP-24 h and pGP-1 week are shown in Fig. 2(f), and all exhibit a predominant C1s peak (286.4 eV) and an O1s peak (532.4 eV).

After exposed to pyrrole monomer, a new N1s peak (399.8 eV) was observed and the peak intensity increased continuously, which indicates the continuous incorporation of pyrrolic-like N atoms [68]. Both the C/O atomic ratios and contents of nitrogen increased over the treatment time (shown in Fig. S6 in the ESM), indicating the removal of oxygen groups from GO sheets and continuous formation of PPy following the SOR reaction. High-resolution C 1s spectra are shown in Fig. 2(g), including C-C/C=C (284.7 eV), C-O-C/C-OH (286.8 eV), C=O (287.7 eV) and HO-C=O (288.9 eV). For the chips treated by pyrrole, a new bond C-N (285.4 eV) was observed, conveying the incorporation of N source. The peak intensity of C-C/C=C and C-N increased over the treatment time while the peak intensity of C-O-C/C-OH and C=O decreased, which is due to the partial reduction of GO and anchoring of nitrogen source (PPy). Calculated from the results of the high-resolution C 1s spectra, the contents of different kinds of C bonds are plotted in Fig. 2(h) (detail contents see Table S1 in the ESM). The figure further proves that the C-O-C/C-OH and C=O groups on GO mainly participated in the SOR reaction, during which the loading of nitrogen source increased continuously.

After carbonization, the pGP was transformed into NC/rGO. The fabricated MSCs derived from GO, pGP-6 h, pGP-24 h and pGP-1 week were respectively denoted as MSC-rGO, MSC-6 h, MSC-24 h and MSC-1 week. The CV curves in Fig. 3(a) exhibit quasi-rectangular shapes, which indicates the capacitive energy storage mechanism [69]. The response current increased for the samples corresponding to the increased immersion time (Fig. S7 in the ESM). This was in accordance with the area of the curves, indicating the improved capacitance (Fig. S8 in the ESM). Calculated from galvanostatic charge and discharge (GCD) test results (Fig. 3(b)), the capacitances of MSC-rGO, MSC-6 h, MSC-24 h and MSC-1 week are 13.6, 42.9, 95.3 and 128.4 $\text{mF}\cdot\text{cm}^{-2}$, respectively. Specific capacitances under different current densities (from 1 to 5 $\text{mA}\cdot\text{cm}^{-2}$) are plotted in Fig. 3(c), which exhibit considerable capacitance retention even at relative high current density compared with previously reported results (shown in Table S2 in the ESM). The increase of capacitance is ascribed to the following reason: As treating

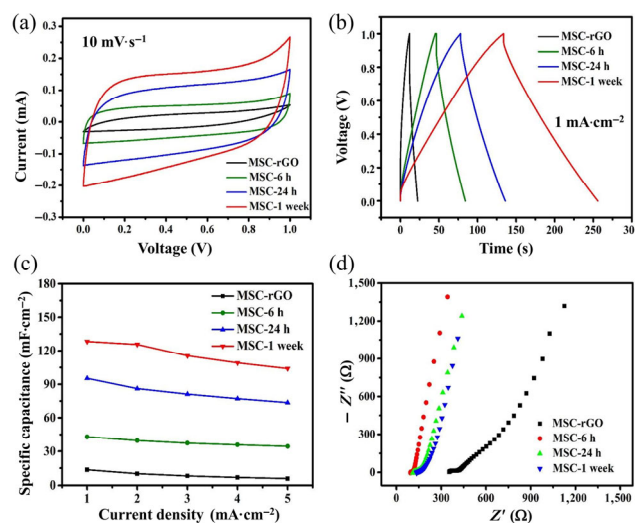


Figure 3 Electrochemical performance of MSCs. (a) CV curves of MSC-rGO, MSC-6 h, MSC-24 h and MSC-1 week at the scan rate of 10 $\text{mV}\cdot\text{s}^{-1}$. (b) GCD curves of MSC-rGO, MSC-6 h, MSC-24 h and MSC-1 week at the current density of 1 $\text{mA}\cdot\text{cm}^{-2}$. (c) Specific capacitances of MSC-rGO, MSC-6 h, MSC-24 h and MSC-1 week calculated from GCD tests results at different current densities. (d) Nyquist plots of MSC-rGO, MSC-6 h, MSC-24 h and MSC-1 week at the frequency range from 0.01 to 5×10^5 Hz.

time increased within 1 week, more PPy was anchored on the micro-patterns, resulting in an increased mass loading of NC after carbonization, resulting in an increased mass loading of NC after carbonization and additional active sites were obtained. In the composite microelectrodes, rGO frameworks acted as conductive skeleton and NC-coating provided abundant active sites for the adsorption/desorption of electrolyte ions. Therefore, the entire system exhibited excellent electronic conductivity and capacitance. The EIS results ranging from 0.01 to 5×10^5 Hz of MSC-rGO, MSC-6 h, MSC-24 h and MSC-1 week are shown in Fig. 3(d). Judging from the simulation results (Fig. S9 in the ESM), the electrodes modified by NC (MSC-6 h, MSC-24 h and MSC-1 week) exhibited lower equivalent series resistance, indicating the improved conductivity after modification [70–72]. In medium-frequency region of the Nyquist plots, the Warburg region decreases with the increase of treating time, indicating more NC covering enhanced the space between graphene layers and facilitated the diffusion of electrolyte ions.

To explore more proper treating time, the printed GO micro-patterns were further treated by liquid pyrrole for 4 days and 2 weeks. The obtained specific capacitances are shown in Fig. S10 in the ESM, in which no obvious improvement was observed with treating time longer than 1 week, indicating the maximum mass loading of NC in this strategy. The change of capacitance before and after O_2 plasma treatment was also investigated (Fig. S11 in the ESM), demonstrating the deeper permeation of electrolyte after treated by O_2 plasma.

The digital image of the fabricated MSC is shown in Fig. 4(a), which shows miniaturized size of around $5 \text{ mm} \times 15 \text{ mm}$ (all 6 finger electrodes). During the printing process, the fibrous GO ink was stacked layer by layer (6 layers in this work), after combined with surface-modification and carbonization processes, NC/rGO-based microelectrodes were finally obtained. Elemental mapping spectra of C, O and N are shown in Fig. 4(b), in which the distribution of N is highly consistent with that of C and O, indicating the successful incorporation of N source. The cross sectional SEM image is presented in Fig. 4(c). The total height of 6 layers is around $946 \mu\text{m}$, this vertically stacked architecture of the microelectrodes achieved a high

mass loading of active materials. Figure 4(d) shows a high-magnification cross sectional SEM image of the filaments. The graphene flakes were obviously aligned with the direction of filaments, owing to the liquid-crystal property of GO inks and the self-orientation during the printing process [23]. The aligned porous structure facilitated the oriented migration of electrolyte ions in microelectrodes. In the SEM images of the electrode surface (Fig. 4(e)), the prominent particles on the rGO surface are supposed to be NC derived from PPy, which provided sufficient active sites for the adsorption/desorption of electrolyte ions. In the higher-magnification cross sectional SEM image of filaments (Fig. 4(f)), graphene flakes are stoutly welded by interconnected NC particles on the edge, which is even more prominent than on the surface of graphene. This difference is caused by the more abundant defects and oxygen-related functional groups on the edge of pristine GO flakes, which provided more anchoring sites for the adsorption of pyrrole and additional NC was accumulated in the final samples. The edge-welded structure strengthened the interface connection of graphene flakes, forming interface-reinforced graphene scaffolds, which enhanced the conductivity and capacitance of the microelectrodes.

As shown in the TEM image (Fig. S12 in the ESM), the crystal/amorphous parts are easy to identify, manifesting that the graphene sheet is modified by NC both on the surface and edge. STEM test was also conducted (shown in Fig. S13 in the ESM) to clearly identify NC and rGO. In Fig. S13(a) in the ESM, thin film with obvious lattice fringe can be identified and the interlamellar distance was measured to be 0.37 nm , this was determined to be rGO. Besides, obvious particles (bright clusters, circled red) can be observed, which was determined to be NC. In Figs. S13(b)–S13(e) in the ESM, the EDS results of C, N and O show high consistency, which indicates successful incorporation of N, and Fig. S13(f) in the ESM also demonstrated an obvious N content.

The surface composition of MSC-1 week was also investigated by XPS and Raman tests. As shown in Fig. 4(g), the survey spectrum exhibits primary peaks of C 1s, N 1s and O 1s. The

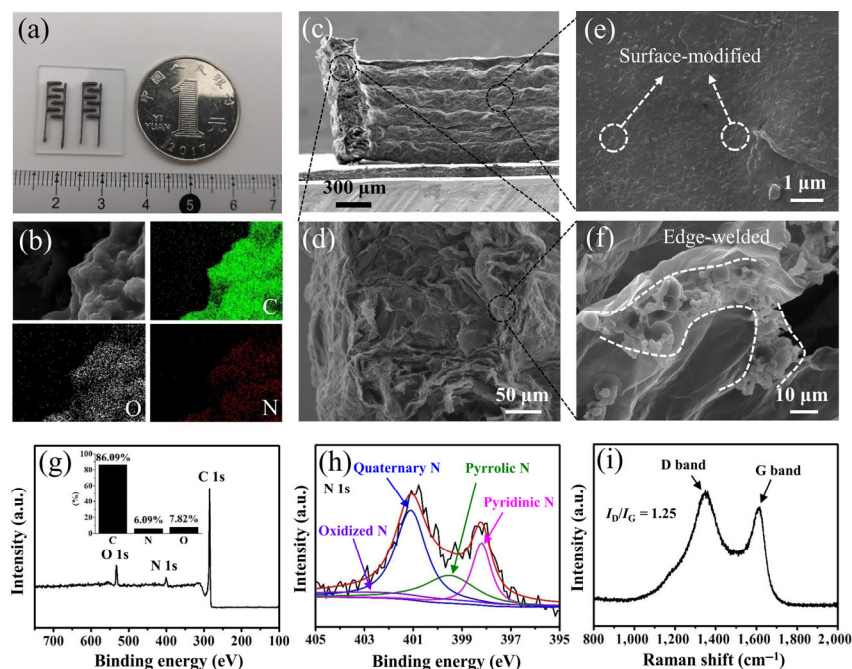


Figure 4 (a) Digital photograph of two printed MSCs and their comparison with a coin. (b) SEM image of the selected part and its corresponding elemental mapping spectra of C, O and N. (c) Lateral SEM image of the stacked filaments. (d) Cross sectional SEM image of the printed filaments. (e) High-magnification SEM image of the surface of graphene. (f) High-magnification image of the cross sectional SEM image. (g) XPS spectrum of MSC-1 week. The inset shows the surface elemental contents of C, N and O. (h) High-resolution N 1s peaks of MSC-1 week. (i) Raman spectrum of MSC-1 week.

inserted image shows that the surface element contents of C, N and O are 86.09%, 6.09% and 7.82%, respectively. The high-resolution N 1s core level spectrum (Fig. 4(h)) suggests four types of nitrogen: pyridinic (398.2 eV), pyrrolic (399.5 eV), quaternary (401.1 eV) and oxidized nitrogen (402.6 eV) [73]. According to previous reports, the pyridinic and pyrrolic N peaks are attributed to the π -conjugated system with a pair of p-electrons, which contributed to the pseudo-capacitance [74]. The Raman spectrum of MSC-1 week is shown in Fig. 4(i), which exhibits typical D band (ca. $1,340\text{ cm}^{-1}$) and G band (ca. $1,585\text{ cm}^{-1}$). The specific value of D and G bands ($I_D/I_G = 1.25$) declares the amorphous form of carbon resulting from the effective carbonization under $800\text{ }^\circ\text{C}$.

MSCs with 3, 12 and 18 layers treated by liquid pyrrole for 1 week were prepared to further demonstrate the potential of this surface engineering strategy (the other parameters remained the same). Due to the different areal mass loading, the obtained specific capacitances tested at $1\text{ mA}\cdot\text{cm}^{-2}$ were 67.9 , 255.2 and $375.4\text{ mF}\cdot\text{cm}^{-2}$, respectively (shown in Fig. S14 in the ESM). The specific capacitance exceeds the previous reported rGO aerogel based MSC ($71.38\text{ mF}\cdot\text{cm}^{-2}$) and putty-like GO derived MSC ($41.2\text{ mF}\cdot\text{cm}^{-2}$) [24, 27]. This result is also comparable with some 3D printed pseudo-MSCs: GO/polyaniline inks derived MSC ($153.6\text{ mF}\cdot\text{cm}^{-2}$) and $\text{V}_2\text{O}_5/\text{VN}$ -based asymmetric MSC ($207.9\text{ mF}\cdot\text{cm}^{-2}$) [28, 29], revealing the high efficiency of the NC-modification. At the current density of $10\text{ mA}\cdot\text{cm}^{-2}$, the MCS with 6 layers exhibits a capacitance retention of 100% even after 10,000 cycles, shown in Fig. 5(a). The GCD curves (left inset) refer to the 1st, 2,500th, 5,000th, 7,500th and 10,000th cycles, which show extremely similar shapes. The right inset refers to an LED lamp powered by four series-connected MSCs. For the samples with 6 layers, compared with MSC-rGO, the areal mass loading of MSC-1 week increased from 4.71 to $7.05\text{ mg}\cdot\text{cm}^{-2}$ owing to the NC modification, whereas the areal capacitance was improved from 13.6 to $128.4\text{ mF}\cdot\text{cm}^{-2}$ (Fig. 5(b)). This declares the crucial significance of NC modification: NC anchored at the edge and surface provided higher conductivity and more sufficient active sites. Calculated from GCD curves at different current densities, the power densities and energy

densities of the sample with 18 layers are plotted in the Ragone plots (Fig. 5(c)). The electrochemical performance is better than the reported GO/polyaniline-ink derived MSC [28], the graphene/phosphorene hybrid films [75], vertically aligned graphene [76], graphene-based in-plane MSC [77], cellular graphene-based MSC [78], hydrated GO-based MSC [9], rGO-based monolithic MSC [79], sulfur-doped graphene-based MSC [80], rGO/Au nanoparticle-based MSC [81] and fully biodegradable MSC [82].

4 Conclusions

An on-chip self-induced selective interface engineering strategy was employed to accurately anchor nitrogen source on the 3D-printed graphene-based microelectrodes. The fabricated edge-welded graphene microelectrode with 6 layers exhibited improved specific areal capacitance from 13.6 to $128.4\text{ mF}\cdot\text{cm}^{-2}$. This spontaneous SOR strategy effectively enhanced the electrochemical performance, and it is highly promising to be widely applied to improve the performance of all types of MSCs derived from GO inks.

Acknowledgements

This work was supported by the National Key Research and Development Program of China (No. 2020YFA715000), the National Natural Science Foundation of China (No. 51802239), the National Key Research and Development Program of China (No. 2019YFA0704902), Foshan Xianhu Laboratory of the Advanced Energy Science and Technology Guangdong Laboratory (Nos. XHT2020-005 and XHT2020-003), the Natural Science Foundation of Hubei Province (No. 2019CFA001), the Fundamental Research Funds for the Central Universities (Nos. 2020III011GX, 2020IVB057, 2019IVB054, 2019III062JL, and 2019-YB-008).

Electronic Supplementary Material: Supplementary material (details of 3D printing process, performance comparison, TEM and STEM measurements) is available in the online version of this article at <https://doi.org/10.1007/s12274-021-3693-4>.

References

- Beidaghi, M.; Gogotsi, Y. Capacitive energy storage in micro-scale devices: Recent advances in design and fabrication of micro-supercapacitors. *Energy Environ. Sci.* **2014**, *7*, 867–884.
- Kyeremateng, N. A.; Brousse, T.; Pech, D. Microsupercapacitors as miniaturized energy-storage components for on-chip electronics. *Nat. Nanotechnol.* **2017**, *12*, 7–15.
- Tyagi, A.; Tripathi, K. M.; Gupta, R. K. Recent progress in micro-scale energy storage devices and future aspects. *J. Mater. Chem. A* **2015**, *3*, 22507–22541.
- Wu, Z. S.; Feng, X. L.; Cheng, H. M. Recent advances in graphene-based planar micro-supercapacitors for on-chip energy storage. *Nat. Sci. Rev.* **2014**, *1*, 277–292.
- Shi, Y.; Peng, L. L.; Ding, Y.; Zhao, Y.; Yu, G. H. Nanostructured conductive polymers for advanced energy storage. *Chem. Soc. Rev.* **2015**, *44*, 6684–6696.
- Li, M.; Lu, J.; Chen, Z. W.; Amine, K. 30 years of lithium-ion batteries. *Adv. Mater.* **2018**, *30*, 1800561.
- Westover, A. S.; Tian, J. W.; Bernath, S.; Oakes, L.; Edwards, R.; Shabab, F. N.; Chatterjee, S.; Anilkumar, A. V.; Pint, C. L. A multifunctional load-bearing solid-state supercapacitor. *Nano Lett.* **2014**, *14*, 3197–3202.
- Wang, Y. F.; Yuan, H. M.; Zhu, Y. H.; Wang, Z. Q.; Hu, Z. W.; Xie, J. W.; Liao, C. Z.; Cheng, H.; Zhang, F. C.; Lu, Z. G. An all-in-one supercapacitor working at sub-zero temperatures. *Sci. China Mater.* **2020**, *63*, 660–666.

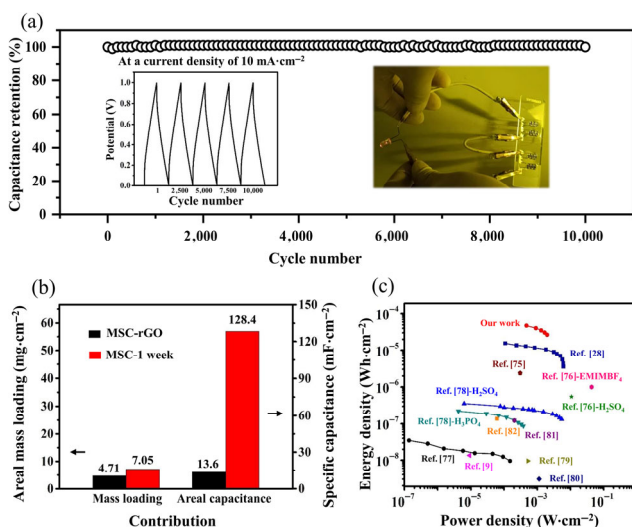


Figure 5 Electrochemical performance of the fabricated MSC-1 week. (a) Cycling performance of MSC-1 week at the current density of $10\text{ mA}\cdot\text{cm}^{-2}$ after 10,000 cycles. The left inset is the GCD curves at 1st, 2,500th, 5,000th, 7,500th and 10,000th cycles. The right inset is a LED lamp powered by four series connected MSCs. (b) The comparison of mass loading and specific capacitance for MSC-rGO and MSC-1 week. (c) Ragone plots of the areal energy densities and power densities of MSC-1 week with 18 layers and their comparison with previously reported results.

- [9] Gao, W.; Singh, N.; Song, L.; Liu, Z.; Reddy, A. L. M.; Ci, L. J.; Vajtai, R.; Zhang, Q.; Wei, B. Q.; Ajayan, P. M. Direct laser writing of micro-supercapacitors on hydrated graphite oxide films. *Nat. Nanotechnol.* **2011**, *6*, 496–500.
- [10] Jiang, Q.; Kurra, N.; Xia, C.; Alshareef, H. N. Hybrid microsupercapacitors with vertically scaled 3D current collectors fabricated using a simple cut-and-transfer strategy. *Adv. Energy Mater.* **2017**, *7*, 1601257.
- [11] Peng, Y. Y.; Akuzum, B.; Kurra, N.; Zhao, M. Q.; Alhabeb, M.; Anasori, B.; Kumbur, E. C.; Alshareef, H. N.; Ger, M. D.; Gogotsi, Y. All-MXene (2D titanium carbide) solid-state microsupercapacitors for on-chip energy storage. *Energy Environ. Sci.* **2016**, *9*, 2847–2854.
- [12] Pu, X.; Liu, M. M.; Li, L. X.; Han, S. C.; Li, X. L.; Jiang, C. Y.; Du, C. H.; Luo, J. J.; Hu, W. G.; Wang, Z. L. Wearable textile-based in-plane microsupercapacitors. *Adv. Energy Mater.* **2016**, *6*, 1601254.
- [13] Cai, J. G.; Lv, C.; Hu, C.; Luo, J. H.; Liu, S.; Song, J. F.; Shi, Y.; Chen, C. G.; Zhang, Z.; Ogawa, S. et al. Laser direct writing of heteroatom-doped porous carbon for high-performance micro-supercapacitors. *Energy Storage Mater.* **2020**, *25*, 404–415.
- [14] Lyu, Z. Y.; Lim, G. J. H.; Guo, R.; Pan, Z. H.; Zhang, X.; Zhang, H.; He, Z. M.; Adams, S.; Chen, W.; Ding, J. et al. 3D-printed electrodes for lithium metal batteries with high areal capacity and high-rate capability. *Energy Storage Mater.* **2020**, *24*, 336–342.
- [15] Yao, B.; Chandrasekaran, S.; Zhang, J.; Xiao, W.; Qian, F.; Zhu, C.; Duoss, E. B.; Spadaccini, C. M.; Worsley, M. A.; Li, Y. Efficient 3D printed pseudocapacitive electrodes with ultrahigh MnO₂ loading. *Joule* **2019**, *3*, 459–470.
- [16] Zhu, C.; Liu, T. Y.; Qian, F.; Han, T. Y. J.; Duoss, E. B.; Kuntz, J. D.; Spadaccini, C. M.; Worsley, M. A.; Li, Y. Supercapacitors based on three-dimensional hierarchical graphene aerogels with periodic macropores. *Nano Lett.* **2016**, *16*, 3448–3456.
- [17] Peng, M. W.; Shi, D. L.; Sun, Y. H.; Cheng, J.; Zhao, B.; Xie, Y. M.; Zhang, J. C.; Guo, W.; Jia, Z.; Liang, Z. Q. et al. 3D printed mechanically robust graphene/CNT electrodes for highly efficient overall water splitting. *Adv. Mater.* **2020**, *32*, 1908201.
- [18] Yao, B.; Chandrasekaran, S.; Zhang, H. Z.; Ma, A. N.; Kang, J. Z.; Zhang, L.; Lu, X. H.; Qian, F.; Zhu, C.; Duoss, E. B. et al. 3D-printed structure boosts the kinetics and intrinsic capacitance of pseudocapacitive graphene aerogels. *Adv. Mater.* **2020**, *32*, 1906652.
- [19] Ambrosi, A.; Pumera, M. Self-contained polymer/metal 3D printed electrochemical platform for tailored water splitting. *Adv. Funct. Mater.* **2018**, *28*, 1700655.
- [20] Ambrosi, A.; Pumera, M. 3D-printing technologies for electrochemical applications. *Chem. Soc. Rev.* **2016**, *45*, 2740–2755.
- [21] Browne, M. P.; Redondo, E.; Pumera, M. 3D printing for electrochemical energy applications. *Chem. Rev.* **2020**, *120*, 2783–2810.
- [22] Egorov, V.; Gulzar, U.; Zhang, Y.; Breen, S.; O'Dwyer, C. Evolution of 3D printing methods and materials for electrochemical energy storage. *Adv. Mater.* **2020**, *32*, 2000556.
- [23] Fu, K.; Wang, Y. B.; Yan, C. Y.; Yao, Y. G.; Chen, Y. N.; Dai, J. Q.; Lacey, S.; Wang, Y. B.; Wan, J. Y.; Li, T. et al. Graphene oxide-based electrode inks for 3D-printed lithium-ion batteries. *Adv. Mater.* **2016**, *28*, 2587–2594.
- [24] Jiang, Y.; Shao, H. B.; Li, C. X.; Xu, T.; Zhao, Y.; Shi, G. Q.; Jiang, L.; Qu, L. T. Versatile graphene oxide putty-like material. *Adv. Mater.* **2016**, *28*, 10287–10292.
- [25] Jiang, Y. Q.; Xu, Z.; Huang, T. Q.; Liu, Y. J.; Guo, F.; Xi, J. B.; Gao, W. W.; Gao, C. Direct 3D printing of ultralight graphene oxide aerogel microlattices. *Adv. Funct. Mater.* **2018**, *28*, 1707024.
- [26] Lacey, S. D.; Kirsch, D. J.; Li, Y. J.; Morgenstern, J. T.; Zarket, B. C.; Yao, Y. G.; Dai, J. Q.; Garcia, L. Q.; Liu, B. Y.; Gao, T. T. et al. Extrusion-based 3D printing of hierarchically porous advanced battery electrodes. *Adv. Mater.* **2018**, *30*, 1705651.
- [27] Li, W. B.; Li, Y. H.; Su, M.; An, B. X.; Liu, J.; Su, D.; Li, L. H.; Li, F. Y.; Song, Y. L. Printing assembly and structural regulation of graphene towards three-dimensional flexible micro-supercapacitors. *J. Mater. Chem. A* **2017**, *5*, 16281–16288.
- [28] Liu, Y. Q.; Zhang, B. B.; Xu, Q.; Hou, Y. Y.; Seyedin, S.; Qin, S.; Wallace, G. G.; Beirne, S.; Razal, J. M.; Chen, J. Development of graphene oxide/polyaniline inks for high performance flexible microsupercapacitors via extrusion printing. *Adv. Funct. Mater.* **2018**, *28*, 1706592.
- [29] Shen, K.; Ding, J. W.; Yang, S. B. 3D printing quasi-solid-state asymmetric micro-supercapacitors with ultrahigh areal energy density. *Adv. Energy Mater.* **2018**, *8*, 1800408.
- [30] Shen, K.; Mei, H. L.; Li, B.; Ding, J. W.; Yang, S. B. 3D printing sulfur copolymer-graphene architectures for Li-S batteries. *Adv. Energy Mater.* **2018**, *8*, 1701527.
- [31] Tang, X. W.; Zhou, H.; Cai, Z. C.; Cheng, D. D.; He, P. S.; Xie, P. W.; Zhang, D.; Fan, T. X. Generalized 3D printing of graphene-based mixed-dimensional hybrid aerogels. *ACS Nano* **2018**, *12*, 3502–3511.
- [32] Wang, Y. B.; Chen, C. J.; Xie, H.; Gao, T. T.; Yao, Y. G.; Pastel, G.; Han, X. G.; Li, Y. J.; Zhao, J. P.; Fu, K. et al. 3D-printed all-fiber Li-ion battery toward wearable energy storage. *Adv. Funct. Mater.* **2017**, *27*, 1703140.
- [33] Wang, Z. S.; Zhang, Q. E.; Long, S. C.; Luo, Y. X.; Yu, P. K.; Tan, Z. B.; Bai, J.; Qu, B. H.; Yang, Y.; Shi, J. et al. Three-dimensional printing of polyaniline/reduced graphene oxide composite for high-performance planar supercapacitor. *ACS Appl. Mater. Interfaces* **2018**, *10*, 10437–10444.
- [34] Wei, N.; Yu, L. H.; Sun, Z. T.; Song, Y. Z.; Wang, M. L.; Tian, Z. N.; Xia, Y.; Cai, J. S.; Li, Y. Y.; Zhao, L. et al. Scalable salt-templated synthesis of nitrogen-doped graphene nanosheets toward printable energy storage. *ACS Nano* **2019**, *13*, 7517–7526.
- [35] Zhu, C.; Han, T. Y. J.; Duoss, E. B.; Golobic, A. M.; Kuntz, J. D.; Spadaccini, C. M.; Worsley, M. A. Highly compressible 3D periodic graphene aerogel microlattices. *Nat. Commun.* **2015**, *6*, 6962.
- [36] Chen, C. L.; Jiang, J. M.; He, W. J.; Lei, W.; Hao, Q. L.; Zhang, X. G. 3D printed high-loading lithium-sulfur battery toward wearable energy storage. *Adv. Funct. Mater.* **2020**, *30*, 1909469.
- [37] Gao, T. T.; Zhou, Z.; Yu, J. Y.; Zhao, J.; Wang, G. L.; Cao, D. X.; Ding, B.; Li, Y. J. 3D printing of tunable energy storage devices with both high areal and volumetric energy densities. *Adv. Energy Mater.* **2019**, *9*, 1802578.
- [38] Li, X. R.; Li, H. P.; Fan, X. Q.; Shi, X. L.; Liang, J. J. 3D-printed stretchable micro-supercapacitor with remarkable areal performance. *Adv. Energy Mater.* **2020**, *10*, 1903794.
- [39] Qiao, Y.; Liu, Y.; Chen, C. J.; Xie, H.; Yao, Y. G.; He, S. M.; Ping, W. W.; Liu, B. Y.; Hu, L. B. 3D-printed graphene oxide framework with thermal shock synthesized nanoparticles for Li-CO₂ batteries. *Adv. Funct. Mater.* **2018**, *28*, 1805899.
- [40] Tang, X. W.; Zhu, C. L.; Cheng, D. D.; Zhou, H.; Liu, X. H.; Xie, P. W.; Zhao, Q. B.; Zhang, D.; Fan, T. X. Architected leaf-inspired Ni_{0.33}Co_{0.66}S₂/graphene aerogels via 3D printing for high-performance energy storage. *Adv. Funct. Mater.* **2018**, *28*, 1805057.
- [41] Fan, Z. D.; Wei, C. H.; Yu, L. H.; Xia, Z.; Cai, J. S.; Tian, Z. N.; Zou, G. F.; Dou, S. X.; Sun, J. Y. 3D printing of porous nitrogen-doped Ti₃C₂ MXene scaffolds for high-performance sodium-ion hybrid capacitors. *ACS Nano* **2020**, *14*, 867–876.
- [42] Orangi, J.; Hamade, F.; Davis, V. A.; Beidaghi, M. 3D printing of additive-free 2D Ti₃C₂T_x (MXene) ink for fabrication of micro-supercapacitors with ultra-high energy densities. *ACS Nano* **2020**, *14*, 640–650.
- [43] Shen, K.; Li, B.; Yang, S. B. 3D printing dendrite-free lithium anodes based on the nucleated MXene arrays. *Energy Storage Mater.* **2020**, *24*, 670–675.
- [44] Yang, W. J.; Yang, J.; Byun, J. J.; Moissinac, F. P.; Xu, J. Q.; Haigh, S. J.; Domingos, M.; Bissett, M. A.; Dryfe, R. A. W.; Barg, S. 3D printing of freestanding MXene architectures for current-collector-free supercapacitors. *Adv. Mater.* **2019**, *31*, 1902725.
- [45] Yu, L. H.; Fan, Z. D.; Shao, Y. L.; Tian, Z. N.; Sun, J. Y.; Liu, Z. F. Versatile N-doped MXene ink for printed electrochemical energy storage application. *Adv. Energy Mater.* **2019**, *9*, 1901839.
- [46] Cao, D. X.; Xing, Y. J.; Tantratian, K.; Wang, X.; Ma, Y.; Mukhopadhyay, A.; Cheng, Z.; Zhang, Q.; Jiao, Y. C.; Chen, L. et al. 3D printed high-performance lithium metal microbatteries enabled by nanocellulose. *Adv. Mater.* **2019**, *31*, 1807313.
- [47] Lin, X. T.; Wang, J. W.; Gao, X. J.; Wang, S. Z.; Sun, Q.; Luo, J.; Zhao, C. T.; Zhao, Y.; Yang, X. F.; Wang, C. H. et al. 3D printing of free-standing “O₂ breathable” air electrodes for high-capacity and long-life Na–O₂ batteries. *Chem. Mater.* **2020**, *32*, 3018–3027.
- [48] Lyu, Z. Y.; Lim, G. J. H.; Guo, R.; Kou, Z. K.; Wang, T. T.; Guan, C.; Ding, J.; Chen, W.; Wang, J. 3D-printed MOF-derived hierarchically porous frameworks for practical high-energy density Li–O₂ batteries. *Adv. Funct. Mater.* **2019**, *29*, 1806658.

- [49] Zhang, J.; Li, X. L.; Fan, S.; Huang, S. Z.; Yan, D.; Liu, L.; Alvarado, P. V. Y.; Yang, H. Y. 3D-printed functional electrodes towards Zn-air batteries. *Mater. Today Energy* **2020**, *16*, 100407.
- [50] Li, H. P.; Liang, J. J. Recent development of printed micro-supercapacitors: Printable materials, printing technologies, and perspectives. *Adv. Mater.* **2020**, *32*, 1805864.
- [51] Wang, Q.; Yan, J.; Fan, Z. J. Carbon materials for high volumetric performance supercapacitors: Design, progress, challenges and opportunities. *Energy Environ. Sci.* **2016**, *9*, 729–762.
- [52] Shi, R. Y.; Han, C. P.; Duan, H.; Xu, L.; Zhou, D.; Li, H. F.; Li, J. Q.; Kang, F. Y.; Li, B. H.; Wang, G. X. Redox-active organic sodium anthraquinone-2-sulfonate (AQS) anchored on reduced graphene oxide for high-performance supercapacitors. *Adv. Energy Mater.* **2018**, *8*, 1802088.
- [53] Xu, L.; Shi, R. Y.; Li, H. F.; Han, C. P.; Wu, M. Y.; Wong, C. P.; Kang, F. Y.; Li, B. H. Pseudocapacitive anthraquinone modified with reduced graphene oxide for flexible symmetric all-solid-state supercapacitors. *Carbon* **2018**, *127*, 459–468.
- [54] Wu, C. X.; Zhang, Z. F.; Chen, Z. H.; Jiang, Z. M.; Li, H. Y.; Cao, H. J.; Liu, Y. S.; Zhu, Y. Y.; Fang, Z. B.; Yu, X. R. Rational design of novel ultra-small amorphous Fe₂O₃ nanodots/graphene heterostructures for all-solid-state asymmetric supercapacitors. *Nano Res.* **2021**, *14*, 953–960.
- [55] Zhang, Y.; Tao, B. L.; Xing, W.; Zhang, L.; Xue, Q. Z.; Yan, Z. F. Sandwich-like nitrogen-doped porous carbon/graphene nanoflakes with high-rate capacitive performance. *Nanoscale* **2016**, *8*, 7889–7898.
- [56] Li, S.; Zhao, C.; Shu, K. W.; Wang, C. Y.; Guo, Z. P.; Wallace, G. G.; Liu, H. K. Mechanically strong high performance layered polypyrrole nano fibre/graphene film for flexible solid state supercapacitor. *Carbon* **2014**, *79*, 554–562.
- [57] Sun, W.; Gao, G. H.; Wu, G. M.; You, Z. W. Surface-oxidation-mediated construction of Ppy@VNO/NG core-shell host targeting highly capacitive and durable negative electrode for supercapacitors. *Sci. China Mater.*, in press, DOI: 10.1007/s40843-020-1607-2.
- [58] Ren, Y. M.; Yu, C. B.; Chen, Z. H.; Xu, Y. X. Two-dimensional polymer nanosheets for efficient energy storage and conversion. *Nano Res.* **2021**, *14*, 2023–2036.
- [59] Tian, X. C.; Shi, M. Z.; Xu, X.; Yan, M. Y.; Xu, L.; Minhas-Khan, A.; Han, C. H.; He, L.; Mai, L. Q. Arbitrary shape engineerable spiral micropseudocapacitors with ultrahigh energy and power densities. *Adv. Mater.* **2015**, *27*, 7476–7482.
- [60] Yang, C. M.; Weidenthaler, C.; Spliethoff, B.; Mayanna, M.; Schüth, F. Facile template synthesis of ordered mesoporous carbon with polypyrrole as carbon precursor. *Chem. Mater.* **2005**, *17*, 355–358.
- [61] Amarnath, C. A.; Hong, C. E.; Kim, N. H.; Ku, B. C.; Kuila, T.; Lee, J. H. Efficient synthesis of graphene sheets using pyrrole as a reducing agent. *Carbon* **2011**, *49*, 3497–3502.
- [62] Gong, F.; Xu, X.; Zhou, G.; Wang, Z. S. Enhanced charge transportation in a polypyrrole counter electrode via incorporation of reduced graphene oxide sheets for dye-sensitized solar cells. *Phys. Chem. Chem. Phys.* **2013**, *15*, 546–552.
- [63] Lu, X. J.; Dou, H.; Yuan, C. Z.; Yang, S. D.; Hao, L.; Zhang, F.; Shen, L. F.; Zhang, L. J.; Zhang, X. G. Polypyrrole/carbon nanotube nanocomposite enhanced the electrochemical capacitance of flexible graphene film for supercapacitors. *J. Power Sources* **2012**, *197*, 319–324.
- [64] Wang, L. C.; Zhang, C. G.; Jiao, X.; Yuan, Z. H. Polypyrrole-based hybrid nanostructures grown on textile for wearable supercapacitors. *Nano Res.* **2019**, *12*, 1129–1137.
- [65] Hassan, H. M. A.; Abdelsayed, V.; Khder, A. E. R. S.; Abouzeid, K. M.; Ternier, J.; El-Shall, M. S.; Al-Resayes, S. I.; El-Azhary, A. A. Microwave synthesis of graphene sheets supporting metal nanocrystals in aqueous and organic media. *J. Mater. Chem.* **2009**, *19*, 3832–3837.
- [66] Bora, C.; Dolui, S. K. Fabrication of polypyrrole/graphene oxide nanocomposites by liquid/liquid interfacial polymerization and evaluation of their optical, electrical and electrochemical properties. *Polymer* **2012**, *53*, 923–932.
- [67] Zhao, Y.; Liu, J.; Hu, Y.; Cheng, H. H.; Hu, C. G.; Jiang, C. C.; Jiang, L.; Cao, A. Y.; Qu, L. T. Highly compression-tolerant supercapacitor based on polypyrrole-mediated graphene foam electrodes. *Adv. Mater.* **2013**, *25*, 591–595.
- [68] Jiang, Y.; Hu, C. G.; Cheng, H. H.; Li, C. X.; Xu, T.; Zhao, Y.; Shao, H. B.; Qu, L. T. Spontaneous, straightforward fabrication of partially reduced graphene oxide-polypyrrole composite films for versatile actuators. *ACS Nano* **2016**, *10*, 4735–4741.
- [69] Simon, P.; Gogotsi, Y. Materials for electrochemical capacitors. *Nat. Mater.* **2008**, *7*, 845–854.
- [70] Ma, T.; Gao, H. L.; Cong, H. P.; Yao, H. B.; Wu, L.; Yu, Z. Y.; Chen, S. M.; Yu, S. H. A bioinspired interface design for improving the strength and electrical conductivity of graphene-based fibers. *Adv. Mater.* **2018**, *30*, 1706435.
- [71] Miao, J. L.; Liu, H. H.; Li, Y. B.; Zhang, X. X. Biodegradable transparent substrate based on edible starch-chitosan embedded with nature-inspired three-dimensionally interconnected conductive nanocomposites for wearable green electronics. *ACS Appl. Mater. Interfaces* **2018**, *10*, 23037–23047.
- [72] Yang, Y. C.; Kim, N. D.; Varshney, V.; Sihm, S.; Li, Y. L.; Roy, A. K.; Tour, J. M.; Lou, J. *In situ* mechanical investigation of carbon nanotube-graphene junction in three-dimensional carbon nanostructures. *Nanoscale* **2017**, *9*, 2916–2924.
- [73] You, B.; Wang, L. L.; Yao, L.; Yang, J. Three dimensional N-doped graphene-CNT networks for supercapacitor. *Chem Commun.* **2013**, *49*, 5016–5018.
- [74] Sheng, Z. H.; Shao, L.; Chen, J. J.; Bao, W. J.; Wang, F. B.; Xia, X. H. Catalyst-free synthesis of nitrogen-doped graphene via thermal annealing graphite oxide with melamine and its excellent electrocatalysis. *ACS Nano* **2011**, *5*, 4350–4358.
- [75] Xiao, H.; Wu, Z. S.; Chen, L.; Zhou, F.; Zheng, S. H.; Ren, W. C.; Cheng, H. M.; Bao, X. H. One-step device fabrication of phosphorene and graphene interdigital micro-supercapacitors with high energy density. *ACS Nano* **2017**, *11*, 7284–7292.
- [76] Zheng, S. H.; Li, Z. L.; Wu, Z. S.; Dong, Y. F.; Zhou, F.; Wang, S.; Fu, Q.; Sun, C. L.; Guo, L. W.; Bao, X. H. High packing density unidirectional arrays of vertically aligned graphene with enhanced areal capacitance for high-power micro-supercapacitors. *ACS Nano* **2017**, *11*, 4009–4016.
- [77] Wu, Z. S.; Parvez, K.; Feng, X. L.; Müllen, K. Graphene-based in-plane micro-supercapacitors with high power and energy densities. *Nat. Commun.* **2013**, *4*, 2487.
- [78] Shao, Y. L.; Li, J. M.; Li, Y. G.; Wang, H. Z.; Zhang, Q. H.; Kaner, R. B. Flexible quasi-solid-state planar micro-supercapacitor based on cellular graphene films. *Mater. Horiz.* **2017**, *4*, 1145–1150.
- [79] Wang, S.; Wu, Z. S.; Zheng, S. H.; Zhou, F.; Sun, C. L.; Cheng, H. M.; Bao, X. H. Scalable fabrication of photochemically reduced graphene-based monolithic micro-supercapacitors with superior energy and power densities. *ACS Nano* **2017**, *11*, 4283–4291.
- [80] Wu, Z. S.; Tan, Y. Z.; Zheng, S. H.; Wang, S.; Parvez, K.; Qin, J. Q.; Shi, X. Y.; Sun, C. L.; Bao, X. H.; Feng, X. L. et al. Bottom-up fabrication of sulfur-doped graphene films derived from sulfur-annulated nanographene for ultrahigh volumetric capacitance micro-supercapacitors. *J. Am. Chem. Soc.* **2017**, *139*, 4506–4512.
- [81] Li, R. Z.; Peng, R.; Kihm, K. D.; Bai, S.; Bridges, D.; Tumuluri, U.; Wu, Z.; Zhang, T.; Compagnini, G.; Feng, Z. et al. High-rate in-plane micro-supercapacitors scribed onto photo paper using *in situ* femtosecond laser-reduced graphene oxide/Au nanoparticle microelectrodes. *Energy Environ. Sci.* **2016**, *9*, 1458–1467.
- [82] Lee, G.; Kang, S. K.; Won, S. M.; Gutruf, P.; Jeong, Y. R.; Koo, J.; Lee, S. S.; Rogers, J. A.; Ha, J. S. Fully biodegradable micro-supercapacitor for power storage in transient electronics. *Adv. Energy Mater.* **2017**, *7*, 1700157.